Surface Ferromagnetism of FeO Nanoparticles Revealed by *Operando* Magnetoelectrochemical Measurements

Hengjun Liu,[1,‡] Fangchao Gu,[1,‡] Xiancheng Sang,[1] Yuanyuan Han,[1] Feihu Zou,[1] Zhaohui Li,[1] Yufeng Qin,[2,†] Li Cai,[3] Yuanyuan Pan,[1] Qiang Cao,[3] Guo-xing Miao,[4] and Qiang Li[1,*]

[1] *College of Physics, Weihai Innovation Research Institute, Qingdao University, Qingdao 266071, China*

[2] *College of Information Science and Engineering, Shandong Agricultural University, Taian, Shandong, 271018, People's Republic of China*

[3] *Spintronics Institute, University of Jinan, Jinan 250022, China*

[4] *Department of Electrical and Computer Engineering & Institute for Quantum Computing, University of Waterloo, Ontario N2L 3G1, Canada*

(Received 12 May 2022; revised 15 February 2023; accepted 4 April 2023; published 5 May 2023)

In view of the long-standing controversy over the surface ferromagnetism of FeO, we propose to prepare its nanoparticles based on the lithium-battery reaction mechanism and carry out *operando* magnetometry measurements. This *operando* magnetoelectrochemical technology allows accurate magnetic detection of electrochemical synthesis products, effectively avoiding various intractable surface reactions during sample transmission processes. Due to the large surface area of nanosized FeO, the magnetometry measurements show strong ferromagnetism and a high Curie temperature of 754 K, which can be attributed to surface frustration and the surface-bulk exchange interaction. These critical results confirm the surface ferromagnetism of FeO and provide valuable insights toward the design of spintronic devices.

DOI: 10.1103/PhysRevApplied.19.054022

I. INTRODUCTION

During the past decades, the surface of iron oxides has attracted increasing attention for sensors, energy devices, hydrogen storage, and biomedicine, due to its electrochemical properties, magnetic features, biocompatibility, and catalytic activity [1–4]. Especially, various spintronic devices with Fe-oxide heterostructures usually reveal slight oxidation of the Fe layer to generate an iron oxide surface due to the influence of atomic diffusion or annealing conditions; this has a significant impact on the device [5–10]. Therefore, there is increasing interest in studying the magnetic properties of such iron oxide surfaces [11–13]. Among numerous iron oxides, FeO is usually regarded as a typical antiferromagnetic material ($T_N \approx 198$ K) [14]. However, previous studies showed that the magnetism of its surface might be different from that of the bulk phase because of the change in surface symmetry and the decrease of some atoms or rows [11,15].

To clarify the magnetic properties of the FeO surface, a large number of theoretical calculations and experiments have been explored [11,16–18]. By comparing the density of states (DOS) of the FeO(111) surface with the bulk, Gao and co-workers revealed that the FeO(111) surface with the NaCl phase had ferromagnetic order [19]. In addition, results based on *ab initio* calculations reflect that the FeO surface exhibits a net magnetic moment due to surface frustration and the surface-bulk exchange interaction [20]. Experimentally, Koike and Furukawa reported ferromagnetic order at the FeO(111) surface by analyzing spin-polarized secondary-electron spectroscopy [14]. Subsequently, the results of the transformation of the FeO surface into Fe_3O_4 through x-ray absorption spectroscopy and magnetic circular dichroism were reported by Vescovo and co-workers, which led to great controversy over the surface ferromagnetism of FeO [21]. The main reason is that, on one hand, the preparation of high-quality samples is challenging. The purity and properties of FeO are always affected by the surrounding atmosphere, temperature, film thickness, and substrates [22–26]. Especially, Fe_3O_4 tends to be formed on FeO films when the thickness reaches several monolayers [21,25,27–29]. On the other hand, the intrinsic properties are well concealed due to the inevitable surface reactions caused by sample transmission or measurement in the atmospheric environment. So it is essential to explore an alternative preparation method and persuasive measurements to investigate the magnetism of the FeO surface.

Theoretically, when the material is prepared in nanosize with high specific areas, surface magnetism will be

*liqiang@qdu.edu.cn

†qinyufeng@sdau.edu.cn

‡H. Liu and F. Gu contributed equally to this work.

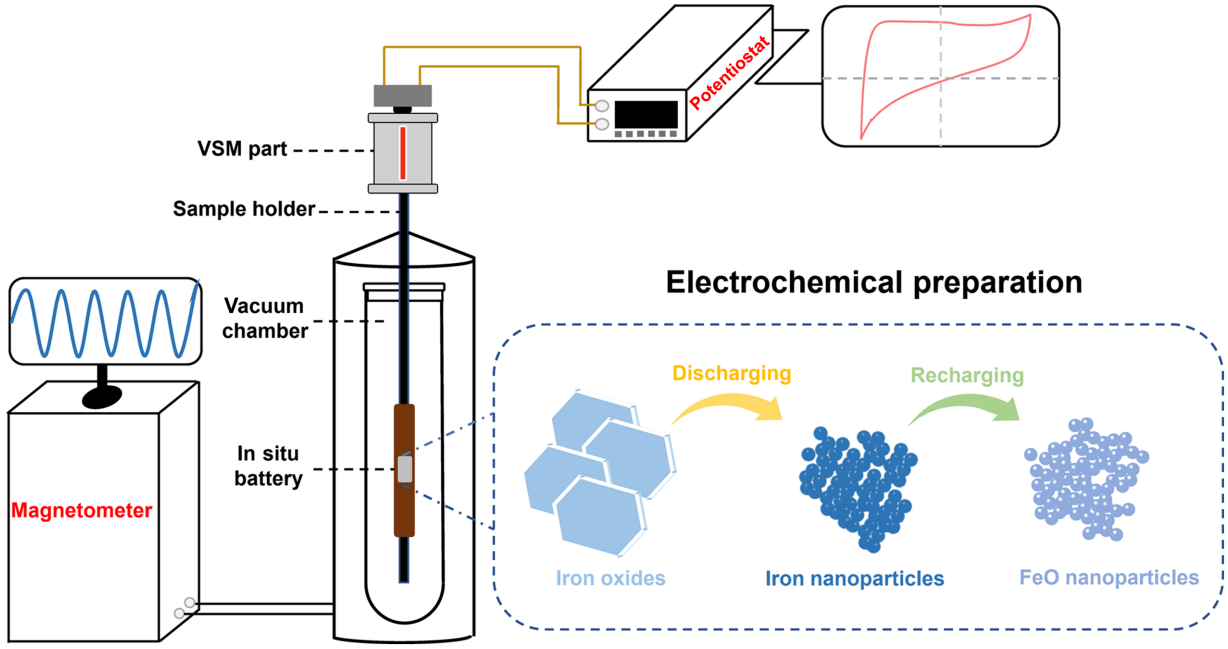

FIG. 1. Schematic diagram of electrochemical synthesis combined with *operando* magnetometry device.

dominant [30–32]. Nanosized FeO can be prepared by electrochemical methods, that is, as the oxidation product of iron oxide electrodes after the lithium battery is fully charged, as demonstrated by various means, such as *in situ* transmission electron microscopy (TEM) and electron energy-loss spectroscopy [33–42]. Herein, this widely recognized *in situ* electrochemical preparation method is combined with *operando* magnetometry to investigate the surface magnetic properties of FeO. A schematic diagram of the device is shown in Fig. 1. *Operando* magnetometry of the preparation process can ensure that FeO is free from intractable surface reactions due to environmental modification. Herein, γ-Fe_2O_3, α-Fe_2O_3, FeS_2, and $FeSe_2$ nanoparticles, and iron oxide thin film, are prepared and then are used as electrodes to investigate the magnetism of FeO nanoparticles, excluding the influence of residual γ-Fe_2O_3, Fe, and additives. Based on the experiment results, we confirm the obvious room-temperature ferromagnetism of the FeO surface. In addition, the Curie temperature (754 K) of as-prepared FeO nanoparticles is calculated from the temperature dependence of magnetization curves.

II. MATERIAL CHARACTERISTICS AND MAGNETIC PROPERTIES

γ-Fe_2O_3 nanoparticles are synthesized by a traditional hydrothermal method, and x-ray diffraction (XRD) using a Cu $K\alpha$ radiation source is used to study its crystal structure. In Fig. 2(a), all diffraction peaks are the same as those of γ-Fe_2O_3 with an inverse-spinel structure, showing the samples do not contain impurities. Then we prepare electrodes composed of γ-Fe_2O_3 nanoparticles, super P (conductive additive), and sodium carboxymethyl cellulose (binders) in a weight ratio of 7:2:1. The battery is assembled in an Ar-filled glove box with the electrode as an anode and lithium metal as a counter electrode, and then this installed in a special testing rod of *operando* magnetometry. The measurements are performed during the charging-discharging process with a voltage range of 0–3 V. According to the electrochemical process reported previously [34,43], the electrochemical reaction of Fe_2O_3 electrodes in a lithium-ion battery during the charge-discharge process can be expressed as

$$Fe_2O_3 + 6Li^+ + 6e^- \Rightarrow 2Fe + 3Li_2O(\text{first discharge}), \quad (1)$$

$$Fe + Li_2O \Rightarrow FeO + 2Li^+ + 2e^-(\text{first charge}), \quad (2)$$

$$FeO + 2Li^+ + 2e^- \Leftrightarrow Fe + Li_2O(\text{subsequent cycles}). \quad (3)$$

Therefore, FeO nanoparticles can be obtained at 3 V in the charging process. To further verify the reliability of the electrochemical preparation of FeO, x-ray photoelectron spectroscopy (XPS) analysis is performed to obtain the valence state of Fe [see Fig. 2(b)]. The Fe 2*p* spectrum displays two major peaks at 722.7 and 709.6 eV, corresponding to Fe^{2+} $2p\,1/2$ and Fe^{2+} $2p_{3/2}$ of FeO [44]. The high-resolution (HR) TEM image shown in Fig. 2(c) reveals a lattice fringe with a *d* spacing of approximately 0.25 nm, which corresponds to the (111) lattice plane of FeO. From the selected-area electron diffraction (SAED) patterns of the electrode [see Fig. 2(d)], the diffraction rings can be identified as the (110), (012), (024), and (220)

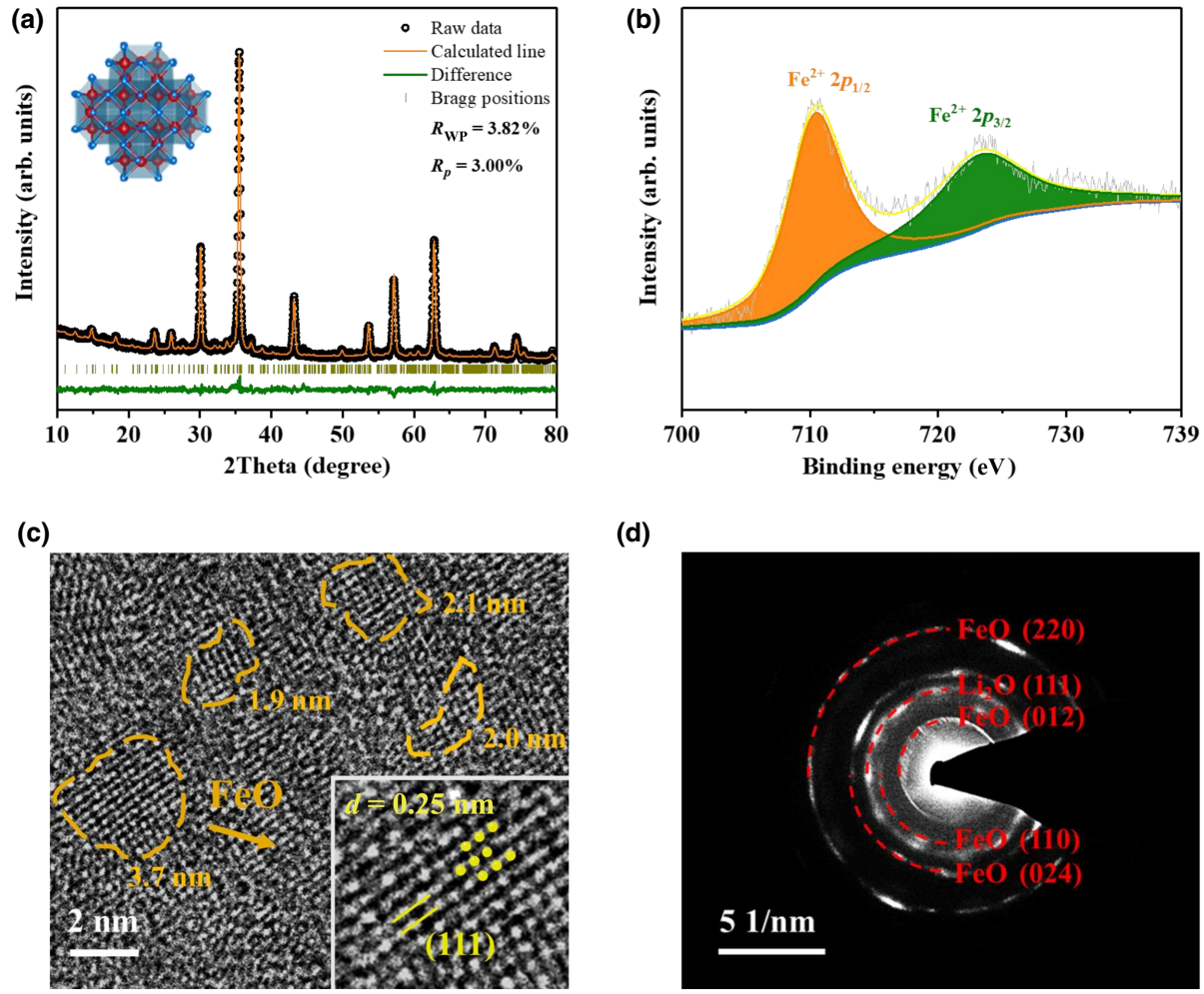

FIG. 2. (a) XRD patterns of γ-Fe_2O_3 nanoparticles. (b) X-ray photoelectron spectra of the oxidation products at 3 V. (c) HRTEM image and (d) SAED pattern of the oxidation products at 3 V under conditions of complete avoidance of oxygen.

lattice planes of FeO [43]. The aforementioned results verify that FeO prepared by the electrochemical method is pure. Residual Li_2O [corresponding to the diffraction ring of (111) in Fig. 2(d)] is due to the irreversible formation of Fe_2O_3 during recharging [43]. To be clear, Li_2O with electrochemically inactive and room-temperature paramagnetism means that the magnetic signal obtained by *operando* magnetometry will be entirely from FeO [43,45].

As shown in Fig. 3(a), the magnetic hysteresis (M-H) curves under different potentials [uncycled (pristine materials), 0 V, 3 V] are evaluated by *operando* magnetometry at room temperature (300 K). The apparent magnetic moment of pristine materials is due to the antiferromagnetic coupling of Fe^{3+} at A (Wyckoff 8a site) and B (Wyckoff 16d site) sites in inverse-spinel γ-Fe_2O_3 [46]. The maximum magnetic moment of FeO (charged to 3 V) is 0.71 μB Fe^{-1} at an external magnetic field of 30 000 Oe, which is different from the pristine materials and reduction products of Fe (discharged to 0 V). Similar M-H curves are obtained at 3 V during different cycles, and the enlarged patterns at the small field are shown in Fig. 3(b). The obvious coercivity is about 21 Oe, indicating the ferromagnetism of the FeO nanoparticles at room temperature.

Since FeO nanoparticles are the oxidation products of Fe nanoparticles, a rough geometric estimate of the proportion of surface FeO can be obtained from the average particle size of Fe. Considering that the Langevin-function fitting method can reflect the overall average nanoparticle size macroscopically, we combine it with the *in situ* device (lithium-ion battery) to estimate the size of Fe nanoparticles more accurately, which can further eliminate the interference of external factors, such as oxygen exposure [47]. According to the M-H curves shown in Fig. 3(a), the average size of Fe nanoparticles can be estimated by fitting the modified Langevin function [48]:

$$M = M_0 L(\mu_P H/kT) + \chi_a H. \quad (4)$$

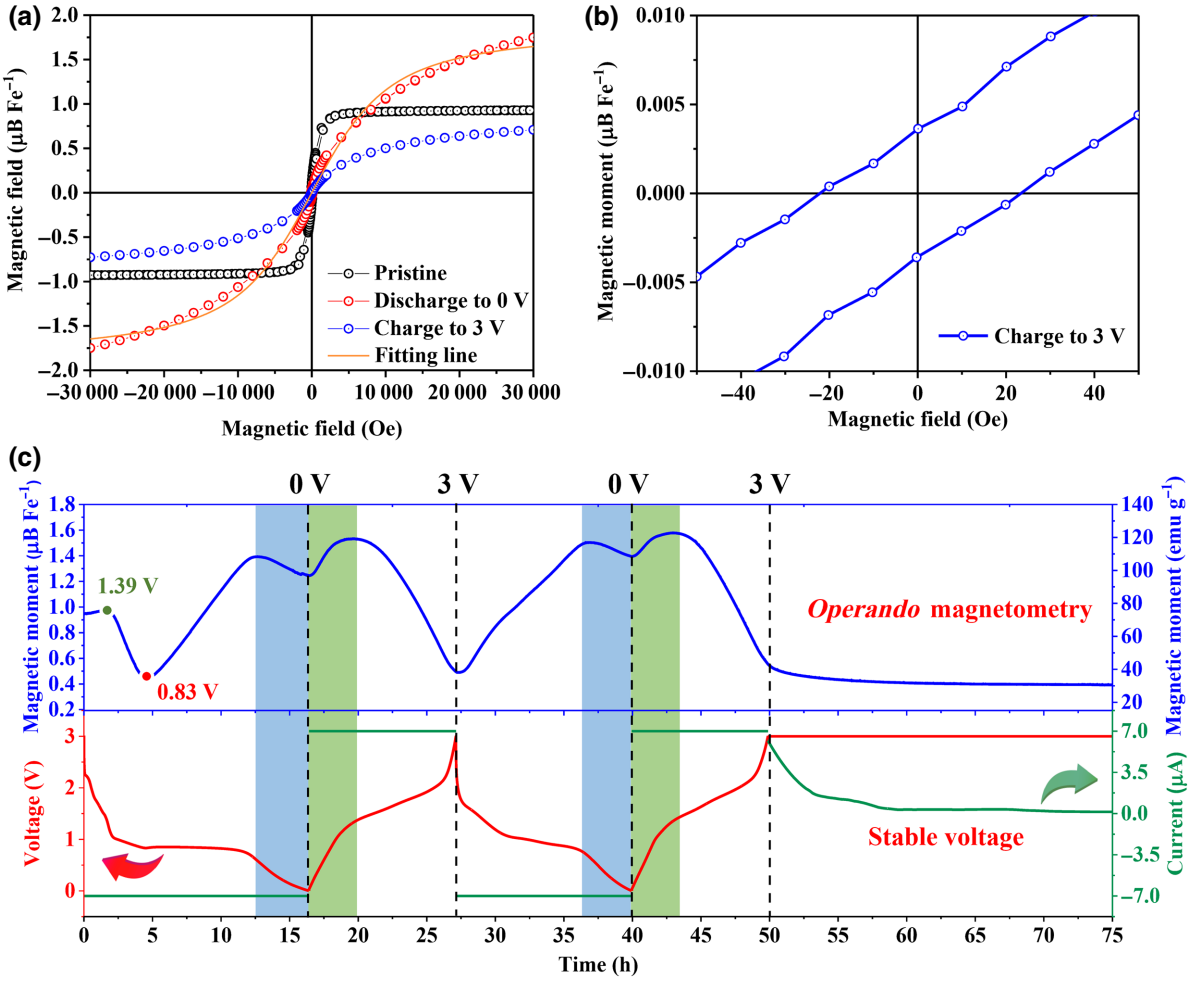

FIG. 3. (a) Magnetic hysteresis curves of the γ-Fe_2O_3 electrode under different potentials [uncycled (pristine materials), 0 V, 3 V] by *operando* magnetometry at room temperature. (b) Low-magnetic-field view. (c) Evolution of magnetization with the galvanostatic charge-discharge mode at a current density of 100 mA g^{-1} under 30 000 Oe at room temperature. After fully charging to 3 V, the current source is set to a regulated mode to maintain voltage stability.

In the formula, $L(x) = \coth - (1/)$ and μ_P is the magnetic moment of each particle. Fitting M-H measurement data with the Langevin function, we find $\mu_P = 1092\ \mu$B. Considering the lattice constant of the Fe bcc unit cell is 0.287 nm, the fitting-average particle diameter of 2.24 nm can be obtained, which is approximately equal to 10 Fe atoms. The proportion of surface iron atoms in a particle can then be calculated by

$$\text{surface atomic ratio}\ (\%) = \frac{S}{T} = \frac{4\pi r^2}{(4/3)\pi r^3}, \qquad (5)$$

where S and T represent the number of iron atoms on the surface and the total number of atoms in the particle, respectively. According to the calculation results, about 60% of the atoms occupy the particle surface, which can also be connected to FeO to illustrate the dominance of surface magnetism. Thus, the observed ferromagnetism of FeO nanoparticles should originate from the FeO surface.

Under an applied magnetic field of 30 000 Oe, the evolution of the magnetization is performed combined with the galvanostatic charge-discharge process. To ensure completion of the reaction, the galvanostatic charge-discharge process of the battery occurs at a tiny current density (100 mAh g^{-1}), and is maintained at 3 V for a long time after two stable cycles to explore the ferromagnetic stability of FeO. Notably, the overall variation of the magnetic moment during the first discharge process is slightly different from that of subsequent processes, which can be caused by the formation of the solid-electrolyte interphase and the irreversible structural changes in the first discharge process. The magnetic increase (initial status to the green point) and subsequent magnetic decrease (green point to the red point) occurring in the first discharge can be attributed to antiferromagnetic coupling between the Fe

ions at *A* and *B* sites of inverse-spinel γ-Fe_2O_3 [33,49]. Namely, the transformation of high-spin Fe^{3+} (5 μB) to low-spin Fe^{2+} (4 μB) at *A* sites and the migration of Fe^{2+} to *B* sites result in the magnetic moment increase. Subsequently, the magnetic moment sharply decreases due to the reduction of Fe^{3+} to Fe^{2+} at *B* sites [33,46,50,51]. Upon further discharge, the occurrence of the conversion reaction induces the reduction of Fe, resulting in a further sharp increase in magnetization ($\Delta M = 0.95$ μB Fe^{-1}). In view of the job-sharing mechanism at low potential, spin-polarized electrons gradually fill in the Fe nanoparticles and Li ions are stored on the surface of Li_2O nanoparticles, forming a space-charge region, which leads to the magnetic moment decreasing (blue region). During charging, the gradual release of spin-polarized electrons from Fe/Li_2O results in a reversible rise in magnetism (green region). Further charging triggers the transformation of Fe into FeO, resulting in a decrease in magnetization. The magnetic variation is highly coupled with the electrochemical process, indicating that the high magnetic moment at 3 V (0.49 μB Fe^{-1}) originates from the ferromagnetism of FeO. After two cycles, the highly reversible magnetization curve confirms that FeO still maintains a high magnetic moment (0.52 μB Fe^{-1}). Although there are some organic and inorganic products (Li_2CO_3, LiF, $ROCO_2Li$, etc.) produced in the electrochemical method, analysis of the magnetic measurements resulting from them can be negligible because of the low content and paramagnetism or nonmagnetism compared with the ferromagnetism of FeO. Then, a voltage-stabilized charging mode is set for the battery and *operando* magnetometry is performed for up to 25 h. We find that the magnetization remains highly stable, which means that the electrochemical reaction for preparing FeO is complete, and the magnetic measurement results are completely derived from FeO.

To further exclude the magnetic moment measured at 3 V from unreacted γ-Fe_2O_3, we also prepare antiferromagnetic α-Fe_2O_3 nanoparticles as the electrode material to further determine the ferromagnetic source observed at 3 V (see Fig. S1 within the S upplemental Material) [52]. Similarly, as shown in Fig. 4(a), the *M*-*H* curves are also measured at the same three voltages. Unlike

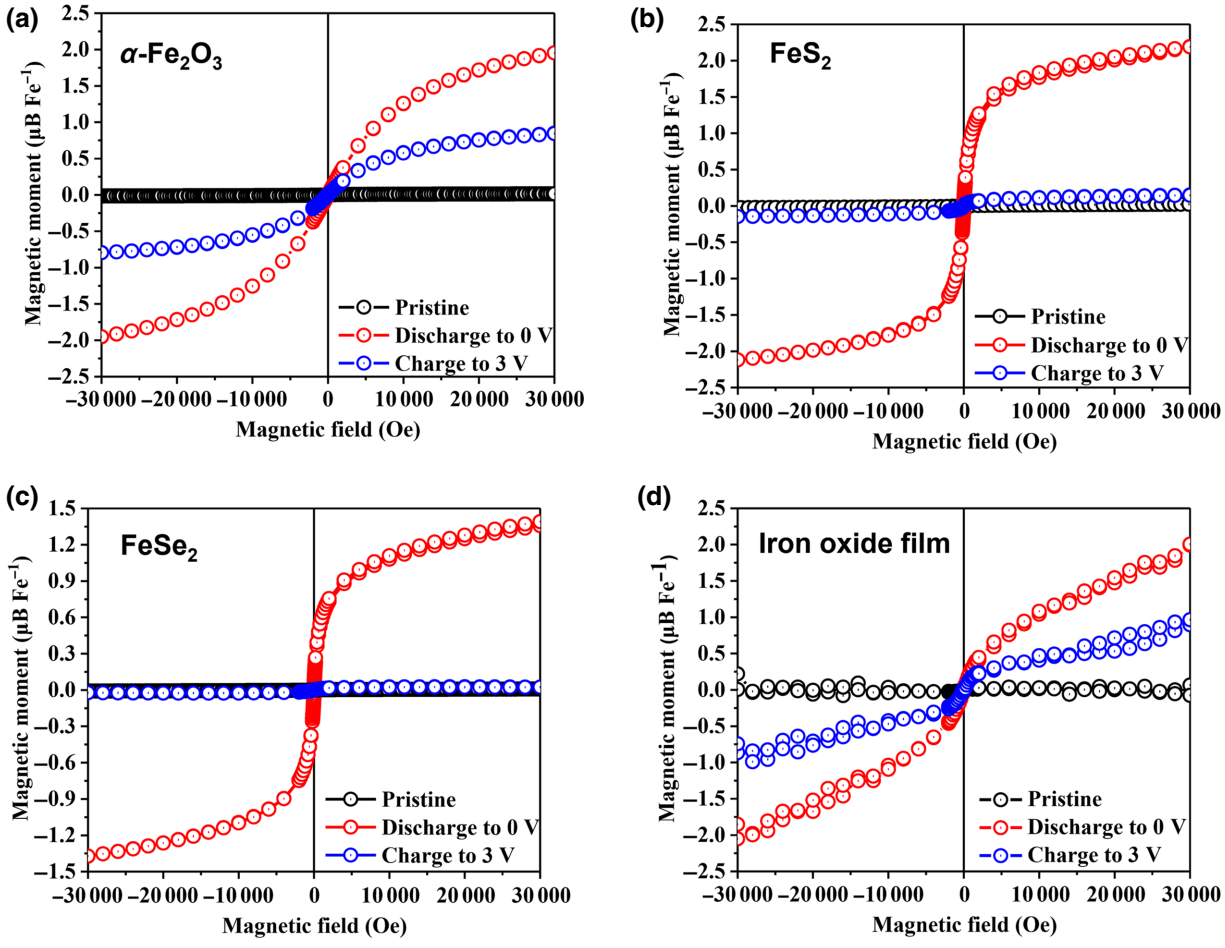

FIG. 4. Magnetic hysteresis curves of (a) α-Fe_2O_3, (b) FeS_2, (c) $FeSe_2$, and (d) iron oxide film electrodes under different potentials [uncycled (pristine materials), 0 V, 3 V] by *operando* magnetometry at room temperature.

γ-Fe_2O_3, the initial magnetic moment of α-Fe_2O_3 is nearly zero. When the potential decreases to 0 V, the maximum magnetic moment rises to 1.95 $\mu B\,Fe^{-1}$, because α-Fe_2O_3 is reduced to Fe during the discharging process. As the potential increases to 3 V, the magnetic moment decreases to 0.84 $\mu B\,Fe^{-1}$, which is similar to the results of FeO nanoparticles obtained in the γ-Fe_2O_3 experiment. Therefore, we can conclude that the high magnetization is independent of γ-Fe_2O_3.

According to the reaction equation, the reduction product Fe is a strong ferromagnetic material, so it is also necessary to exclude the possibility that unreacted Fe contributes to the magnetic moment. In addition to proving from the XPS, HRTEM, and SAED results that the magnetic moment is independent of unreacted Fe, we set up comparative experiments to verify it. Owing to the same reduction products of Fe particles, we further prepare FeS_2 and $FeSe_2$ nanoparticles by a similar hydrothermal method (Figs. S2 and S3 within the Supplemental Material) [52–54]. As shown in Figs. 4(b) and 4(c), the *M*-*H* curves are also measured at three voltages for both FeS_2 and $FeSe_2$ electrodes. The *M*-*H* curves of both pristine FeS_2 and $FeSe_2$ exhibit an antiferromagnetism state, which is consistent with previous reports [53,55]. When the discharging potential decreases to 0 V, there is a large increase in the magnetic moment (2.20 and 1.39 $\mu B\,Fe^{-1}$ for FeS_2 and $FeSe_2$, respectively) because of the formation of Fe nanoparticles. However, with recharging to 3 V, the *M*-*H* curves return to the original antiferromagnetic states, which indicates that there are no Fe nanoparticles. Hence, the ferromagnetism in both α-Fe_2O_3 and γ-Fe_2O_3 experiments at 3 V do not originate from ferromagnetic Fe nanoparticles. It is worth noting that the magnetic moment of $FeSe_2$ at 0 V is lower than that of FeS_2. This phenomenon is due to the difference in the size of Fe nanoparticles (Fig. S4 within the Supplemental Material) [52], which causes the magnetic moment to be suppressed by different degrees of thermal disturbance and a job-sharing effect in *operando* magnetometry at room temperature [55–58].

To exclude the possibility that the binders and conductive additives in the electrode interfere with the magnetic measurement results, we prepare 50-nm self-supported paramagnetic iron oxide films by magnetron sputtering at room temperature. From the relative *M*-*H* curves shown in Fig. 4(d), we can see that the magnetic states at different potentials are similar to that of α-Fe_2O_3. At a potential of 3 V, the highest magnetic moment at 30 000 Oe is 0.96 $\mu B\,Fe^{-1}$. Furthermore, the *M*-*H* curves of the battery without active material (the electrode contains only binder and conductive additives) are further recorded and the corresponding evolution of magnetization is investigated. As shown in Fig. S5(a) within the Supplemental Material, compared with the magnetic moments in the other three states [uncycled (pristine materials), 0 V, 3 V], the magnetic moment is very weak when there are only binders and conductive additives on the electrode [52]. Meanwhile, the corresponding battery is further subjected to continuous magnetization sampling with cyclic voltammetry (*CV*) mode at a scan rate of 0.5 $mV\,s^{-1}$. As the voltage changes, its magnetic moment remains stable at a low value [Fig. S5(b) within the Supplemental Material] [52]. These results indicate that the binders and conductive additives have no effect on magnetic variation during the electrochemical process. Based on the above comparative experiments, we can come to the conclusion that the ferromagnetism at 3 V originates only from the FeO nanoparticle surfaces.

Therefore, based on *in situ* magnetometry and comparative experimental results, we further explore on these FeO nanoparticles with a high specific surface area. The magnetization of FeO nanoparticles as a function of temperature (*M*-*T* curves) is measured under field-cold (FC) and zero-field-cold (ZFC) conditions. To obtain ZFC curves, the samples are first cooled to 8 K in zero magnetic field, and then a small external magnetic field of 100 Oe is applied during the whole measuring process from 8 to 300 K. While for the FC curves, the sample is cooled to 8 K with a small external magnetic field of 100 Oe, and then data are recorded following the same process as that used for the ZFC curves. As shown in Fig. 5(a), there is an obvious splitting between ZFC and FC magnetization curves, corresponding to the existence of superparamagnetism induced by the nanoeffect [59,60]. It is generally believed that the peak value of the ZFC curve corresponds to the blocking temperature (T_B) of the particles, and the blocking temperature is proportional to the sizes of the particles. However, a broad blocking-temperature peak in the range of 50–100 K, rather than a sharp peak in our ZFC curve, corresponds to the broad size distribution of as-prepared FeO [57].

The *M*-*T* curves (blue scattered line) under a magnetic field of 30 000 Oe are also measured from 8 to 300 K, as shown in Fig. 5(b). We also show the reciprocal magnetic susceptibility, depending on temperature (χ^{-1} - *T*, red scattered line) in Fig. 5(b). Data from 100 to 300 K are fitted by the Curie-Weiss law as follows [61,62]:

$$\chi = \frac{C}{T - T_C}. \tag{6}$$

The calculated Curie temperature (T_C) of FeO nanoparticles is 754 K.

For ferromagnetic (FM) and antiferromagnetic (AFM) systems, such as nanoparticles with the core coupled to the shell (Co_{core}-CoO_{shell}) [63], the exchange coupling can provide additional uniaxial anisotropy to stabilize magnetization [64–66]. In this case, the *M*-*H* curve of FeO nanoparticles at 5 k is characterized. As shown in Fig. S6 within the Supplemental Material, for FeO nanoparticles

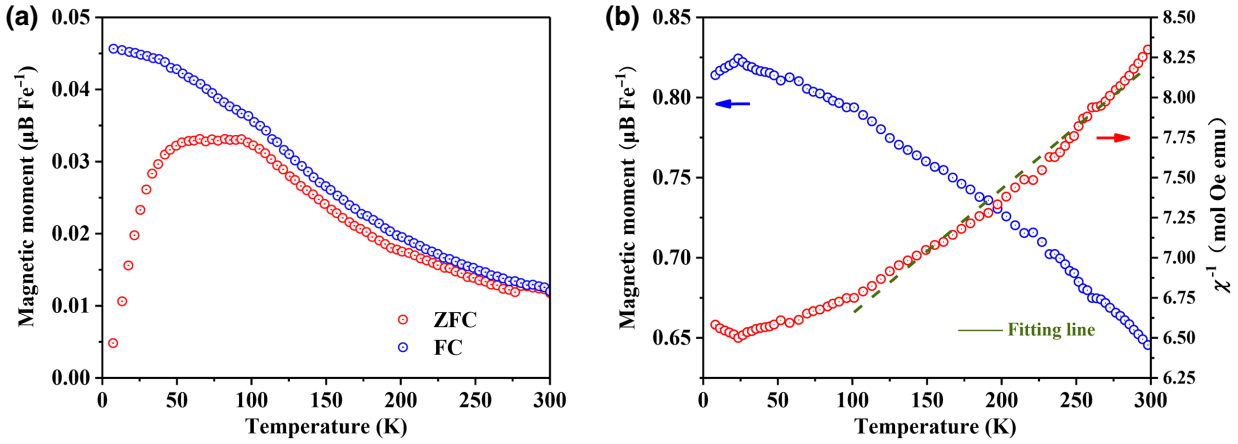

FIG. 5. (a) FC and ZFC curves of FeO nanoparticles under 100 Oe from 8 to 300 K. (b) M-T and χ^{-1}-T curves of FeO nanoparticles under 30 000 Oe from 8 to 300 K, and the green dashed line is the fit using the Curie-Weiss law.

where the core is coupled to shell ($core_{AFM}$-$shell_{FM}$), a hysteresis loop exhibits an exchange bias field of 760 Oe [52]. Therefore, we have reason to believe that the magnetic properties of FeO nanoparticles can be ideally tuned by controlling the ratio of the antiferromagnetic core to the ferromagnetic surface, which will provide an alternative way to design modern magnetic devices.

III. SUMMARY AND CONCLUSIONS

We obtain FeO nanoparticles with a high specific surface area by an electrochemical synthesis method for *operando* magnetometry, which greatly avoids intractable surface reactions caused by environmental modification. The experimental results illustrate that the ferromagnetism of FeO comes from the high proportion of surface. Further investigation shows that the T_C of FeO nanoparticles with a high specific surface area is 754 K. We infer that adjusting the ratio of the FeO surface to core would provide an alternative entry point for regulating the magnetic properties, which is of great significance for the design of various spintronic devices. In addition, the direct combination of the electrochemical synthesis method and *operando* magnetometry can largely avoid the influence of external parameters on intrinsic properties, which will become an effective method for exploring the magnetism of materials.

IV. EXPERIMENT DETAILS

A. Sample preparation

The α-Fe_2O_3 nanoparticles are prepared by a hydrothermal method. First, $FeCl_3{\cdot}6H_2O$ (0.984 g) is dissolved in a mixture of ethanol (36 ml) and water (2.52 ml). After sufficient magnetic stirring, sodium acetate (2.88 g) is added to the above solution and then stirring is continued for 4 h. The obtained red-brown solution is transferred to a Teflon-lined stainless-steel autoclave (50 ml) and heated at 180 °C for 12 h. After cooling to room temperature, the products are centrifuged with deionized water and ethanol and finally dried under vacuum at 60 °C overnight, then the α-Fe_2O_3 nanoparticles are obtained.

To obtain γ-Fe_2O_3 nanoparticles, the as-prepared red-brown α-Fe_2O_3 nanoparticles are calcined at 450 °C for 7 h under an Ar-H_2 atmosphere at a heating rate of 2 °C min^{-1}. Then the black products are annealed at 250 °C for 6 h at a rate of 1 °C min^{-1} under an oxygen atmosphere.

FeS_2 and $FeSe_2$ nanoparticles are prepared by the hydrothermal method reported previously [53,55].

Iron oxide film (50 nm) is prepared on copper foil by direct-current magnetron sputtering with the iron target (99.99%) at room temperature. The sputtering pressure of the argon-oxygen mixture (oxygen content is 20%) is 7.5×10^{-3} Torr.

B. Material characterization

A Rigaku D/Max x-ray diffractometer with Cu $K\alpha$ radiation is used to measure the structures of samples in the range of 2θ (20°–80°). XPS is collected by using a Thermo Scientific ESCALAB 250XI photoelectron spectrometer. HRTEM (JEOL JEM-2100F) and SAED are used to characterize the microstructure of the samples. The above samples for XPS measurements are derived from the following procedures. We disassemble the battery in an Ar-filled glove box and transfer the electrode to the instrument cavity instantly, which greatly avoids interference from oxidation and other factors during the measuring process. To ensure that the entire testing process for HRTEM and SAED for the characterization of FeO is fully completed under an oxygen-free atmosphere, the target electrode is taken out in a manual box filled with argon, and then transferred to the test instrument using a transition chamber.

C. Magnetic measurements

The magnetism of the samples is determined by using a Quantum Design physical property measurement system magnetometer and vibrating sample magnetometer (VSM) at different temperatures. According to the size of the instrument, an *operando* magnetometry auxiliary device is designed by using paramagnetic materials, and the weak background signals are eliminated for all samples. The magnetic measurements are performed simultaneously with cyclic voltammetry, which is performed at a scan rate of 0.5 mV s^{-1} between 0 and 3 V by using a Keithley 2400 source meter at room temperature.

ACKNOWLEDGMENTS

This work is supported partly by the National Natural Science Foundation of China (Grants No. 22179066, No. 11904409, and No. 11974145), the Natural Science Foundation of Shandong Province (Grants No. ZR2020MA073 and No. ZR2020ZD28), and the Project of Shandong Province Higher Educational Science and Technology Program (Grant No. J17KA184).

[1] Lindsay R. Merte, Christopher J. Heard, J. C. Feng Zhang, Mikhail Shipilin, Johan Gustafson, Jason F. Weaver, H. Grönbeck, and E. Lundgren, Tuning the reactivity of ultrathin oxides: NO adsorption on monolayer FeO(111), Angew. Chem., Int. Ed. **55**, 9267 (2016).

[2] J. Ma, X. Guo, Y. Yan, H. Xue, and H. Pang, FeO_x-based materials for electrochemical energy storage, Adv. Sci. **5**, 1700986 (2018).

[3] B. Dieny and M. Chshiev, Perpendicular magnetic anisotropy at transition metal/oxide interfaces and applications, Rev. Mod. Phys. **89**, 025008 (2017).

[4] G. Niraula, J. A. H. Coaquira, F. H. Aragon, A. F. Bakuzis, B. M. G. Villar, F. Garcia, D. Muraca, G. Zoppellaro, A. I. Ayesh, and S. K. Sharma, Stoichiometry and Orientation- and Shape-Mediated Switching Field Enhancement of the Heating Properties of Fe_3O_4 Circular Nanodiscs, Phys. Rev. Appl. **15**, 014056 (2021).

[5] J. M. De Teresa, A. Barthelemy, A. Fert, J. P. Contour, F. Montaigne, and P. Seneor, Role of metal-oxide interface in determining the spin polarization of magnetic tunnel junctions, Science **286**, 507 (1999).

[6] H. X. J. Joshua Yang, Chengxiang Ji, William F. Stickle, Duncan R. Stewart, Douglas A. A. Ohlberg, R. Stanley Williams, and Y. Austin Chang, Origin of inverse tunneling magnetoresistance in a symmetric junction revealed by delaminating the buried electronic interface, Appl. Phys. Lett. **95**, 233117 (2009).

[7] Zhaoqiang Bai, Lei Shen, Qingyun Wu, Minggang Zeng, Jian-Sheng Wang, Guchang Han, and Y. P. Feng, Boron diffusion induced symmetry reduction and scattering in CoFeB/MgO/CoFeB magnetic tunnel junctions, Phys. Rev. B **87**, 014114 (2013).

[8] Z. Wang, M. Saito, K. P. McKenna, S. Fukami, H. Sato, S. Ikeda, H. Ohno, and Y. Ikuhara, Atomic-scale structure and local chemistry of CoFeB-MgO magnetic tunnel junctions, Nano Lett. **16**, 1530 (2016).

[9] A. J. Tan, M. Huang, S. Sheffels, F. Büttner, S. Kim, A. H. Hunt, I. Waluyo, H. L. Tuller, and G. S. D. Beach, Hydration of gadolinium oxide (GdO_x) and its effect on voltage-induced Co oxidation in a Pt/Co/GdO_x/Au heterostructure, Phys. Rev. Mater. **3**, 064408 (2019).

[10] J. Lourembam, X. Yu, M. P. R. Sabino, M. Tran, R. W. T. Ang, Q. J. Yap, S. Ter Lim, and A. Rusydi, Critical Role of Capping Layer in Determining Co-Fe-B/MgO Interfacial Magnetism Revealed by X-Ray Magnetic Circular Dichroism, Phys. Rev. Appl. **14**, 054022 (2020).

[11] A. Schrön and F. Bechstedt, Spin-dependent properties and images of MnO, FeO, CoO, and NiO(001) surfaces, Phys. Rev. B **92**, 165112 (2015).

[12] A. L. Lin, J. N. Rodrigues, C. Su, M. Milletari, K. P. Loh, T. Wu, W. Chen, A. H. Neto, S. Adam, and A. T. Wee, Tunable room-temperature ferromagnet using an iron-oxide and graphene oxide nanocomposite, Sci. Rep. **5**, 11430 (2015).

[13] G. S. Parkinson, Iron oxide surfaces, Surf. Sci. Rep. **71**, 272 (2016).

[14] K. Koike and T. Furukawa, Evidence for Ferromagnetic Order at the FeO(111) Surface, Phys. Rev. Lett. **77**, 3921 (1996).

[15] K. Mori, M. Yamazaki, T. Hiraki, H. Matsuyama, and K. Koike, Magnetism of a FeO(111)/Fe(110)surface, Phys. Rev. B **72**, 014418 (2005).

[16] V. S. C. Kolluru and R. G. Hennig, Role of magnetism on transition metal oxide surfaces in vacuum and solvent, Phys. Rev. Mater. **4**, 045803 (2020).

[17] A. Schrön, C. Rödl, and F. Bechstedt, Crystalline and magnetic anisotropy of the 3*d*-transition metal monoxides MnO, FeO, CoO, and NiO, Phys. Rev. B **86**, 115134 (2012).

[18] G. S. D. Beach, F. T. Parker, D. J. Smith, P. A. Crozier, and A. E. Berkowitz, New Magnetic Order in Buried Native Iron Oxide Layers, Phys. Rev. Lett. **91**, 267201 (2003).

[19] Y. L. Li, K. L. Yao, Z. L. Liu, and G. Y. Gao, First-principles study of the composition, structure, and stability of the FeO(111) surface, Phys. Rev. B **72**, 155446 (2005).

[20] I. Bernal-Villamil and S. Gallego, Structure and magnetism of the-(2 /*times* 2FeO(111) surface, Phys. Rev. B **94**, 075431 (2016).

[21] H.-J. Kim, J.-H. Park, and E. Vescovo, Oxidation of the Fe(110) surface: An Fe_3O_4(111)/Fe(110) bilayer, Phys. Rev. B **61**, 15284 (2000).

[22] M. Monti, B. Santos, A. Mascaraque, O. R. d. l. Fuente, M. A. Niño, T. O. Menteş, A. Locatelli, K. F. McCarty, J. F. Marco, and J. d. l. Figuera, Oxidation pathways in bicomponent ultrathin iron oxide films, J. Phys. Chem. C **116**, 11539 (2012).

[23] M. L. L. Giordano, I. M. N. Groot, Y.-N. Sun, J. Goniakowski, C. Noguera, S. Shaikhutdinov, G. Pacchioni, and H.-J. Freund, Oxygen-induced transformations of an FeO(111) film on Pt(111): A combined DFT and STM study, J. Phys. Chem. C **114**, 21504 (2010).

[24] Y.-N. Sun, Z.-H. Qin, M. Lewandowski, E. Carrasco, M. Sterrer, S. Shaikhutdinov, and H.-J. Freund, Monolayer iron oxide film on platinum promotes low temperature CO oxidation, J. Catal. **266**, 359 (2009).

[25] G. Ketteler and W. Ranke, Heteroepitaxial growth and nucleation of iron oxide films on Ru(0001), J. Phys. Chem. B **107**, 4320 (2003).
[26] W. Ranke, M. Ritter, and W. Weiss, Crystal structures and growth mechanism for ultrathin films of ionic compound materials, Phys. Rev. B **60**, 1527 (1999).
[27] E. Vescovo, Reply to "comment on 'oxidation of the Fe(110) surface: AnFe_3O_4(111)/Fe(110) bilayer'", Phys. Rev. B **74**, 026406 (2006).
[28] A. N. Koveshnikov, R. H. Madjoe, J. Karunamuni, R. L. Stockbauer, and R. L. Kurtz, Oxidized ultrathin Fe films on Cu(001), J. Appl. Phys. **87**, 5929 (2000).
[29] N. G. Condon, F. M. Leibsle, T. Parker, A. R. Lennie, D. J. Vaughan, and G. Thornton, Biphase ordering on Fe_3O_4(111), Phys. Rev. B **55**, 23 (1997).
[30] T. Mizuhara, D. F. Moyano, and V. M. Rotello, Using the power of organic synthesis for engineering the interactions of nanoparticles with biological systems, Nano Today **11**, 31 (2016).
[31] A. Verma and F. Stellacci, Effect of surface properties on nanoparticle-cell interactions, Small **6**, 12 (2010).
[32] C.-F. Lin, E.-Z. Liang, S.-M. Shih, and W.-F. Su, Significance of surface properties of CdS nanoparticles, Jpn. J. Appl. Phys. **42**, L610 (2003).
[33] Q. Li, H. Li, Q. Xia, Z. Hu, Y. Zhu, S. Yan, C. Ge, Q. Zhang, X. Wang, X. Shang *et al.*, Extra storage capacity in transition metal oxide lithium-ion batteries revealed by *in situ* magnetometry, Nat. Mater. **20**, 76 (2020).
[34] W. Zhang, D. C. Bock, C. J. Pelliccione, Y. Li, L. Wu, Y. Zhu, A. C. Marschilok, E. S. Takeuchi, K. J. Takeuchi, and F. Wang, Insights into ionic transport and structural changes in magnetite during multiple-electron transfer reactions, Adv. Energy Mater. **6**, 1502471 (2016).
[35] F. Zhang, Z. Li, Q. Xia, Q. Zhang, C. Ge, Y. Chen, X. Li, L. Zhang, K. Wang, H. Li, *et al.*, Li-ionic control of magnetism through spin capacitance and conversion, Matter **4**, 3605 (2021).
[36] C. N. Lininger, A. M. Bruck, D. M. Lutz, L. M. Housel, K. J. Takeuchi, E. S. Takeuchi, A. Huq, A. C. Marschilok, and A. C. West, The systematic refinement for the phase change and conversion reactions arising from the lithiation of magnetite nanocrystals, Adv. Funct. Mater. **30**, 1907337 (2019).
[37] X. Lv, J. Deng, B. Wang, J. Zhong, T.-K. Sham, X. Sun, and X. Sun, γ-Fe_2O_3@CNTs anode materials for lithium ion batteries investigated by electron energy loss spectroscopy, Chem. Mater. **29**, 3499 (2017).
[38] S. Petnikota, S. K. Marka, A. Banerjee, M. V. Reddy, V. V. S. S. Srikanth, and B. V. R. Chowdari, Graphenothermal reduction synthesis of 'exfoliated graphene oxide/iron (II) oxide' composite for anode application in lithium ion batteries, J. Power Sources **293**, 253 (2015).
[39] W. Li, D. M. Lutz, L. Wang, K. J. Takeuchi, A. C. Marschilok, and E. S. Takeuchi, Peering into batteries: Electrochemical insight through *in situ* and *operando* methods over multiple length scales, Joule **5**, 77 (2021).
[40] X. Hua, P. K. Allan, C. Gong, P. A. Chater, E. M. Schmidt, H. S. Geddes, A. W. Robertson, P. G. Bruce, and A. L. Goodwin, Non-equilibrium metal oxides via reconversion chemistry in lithium-ion batteries, Nat. Commun. **12**, 561 (2021).
[41] C. Nayak, N. Abharana, B. Modak, K. Halankar, S. N. Jha, and D. Bhattacharyya, Insight into the charging-discharging of magnetite electrodes: *In situ* XAS and DFT study, Phys. Chem. Chem. Phys. **23**, 6051 (2021).
[42] C. Colliex, T. Manoubi, and C. Ortiz, Electron-energy-loss-spectroscopy near-edge fine structures in the iron-oxygen system, Phys. Rev. B **44**, 11402 (1991).
[43] Q. Su, D. Xie, J. Zhang, G. Du, and B. Xu, *In situ* transmission electron microscopy observation of the conversion mechanism of Fe_2O_3/graphene anode during lithiation-delithiation processes, ACS Nano **7**, 9115 (2013).
[44] P. S. Bagus, C. J. Nelin, C. R. Brundle, B. V. Crist, N. Lahiri, and K. M. Rosso, Combined multiplet theory and experiment for the Fe $2p$ and $3p$ XPS of FeO and Fe_2O_3, J. Chem. Phys. **154**, 094709 (2021).
[45] F. Beuneu, P. Vajda, O. J. Zogal, D. Massiot, J. P. Coutures, and P. Florian, Low-temperature and high-temperature experiments on electron-irradiated Li_2O: Molecular-oxygen freezing and metallic-lithium melting, Nucl. Instrum. Methods Phys. Res., Sect. B **166**, 270 (2000).
[46] S. Dasgupta, B. Das, M. Knapp, R. A. Brand, H. Ehrenberg, R. Kruk, and H. Hahn, Intercalation-driven reversible control of magnetism in bulk ferromagnets, Adv. Mater. **26**, 4639 (2014).
[47] G. Barrera, P. Allia, and P. Tiberto, Magnetization Dynamics of Superparamagnetic Nanoparticles for Magnetic Particle Spectroscopy and Imaging, Phys. Rev. Appl. **18**, 024077 (2022).
[48] A. Punnoose, T. Phanthavady, M. S. Seehra, N. Shah, and G. P. Huffman, Magnetic properties of ferrihydrite nanoparticles doped with Ni, Mo, and Ir, Phys. Rev. B **69**, 054425 (2004).
[49] C. C. Chen and J. Maier, Decoupling electron and ion storage and the path from interfacial storage to artificial electrodes, Nat. Energy **3**, 102 (2018).
[50] T. Yamada, K. Morita, K. Kume, H. Yoshikawa, and K. Awaga, The solid-state electrochemical reduction process of magnetite in Li batteries: *In situ* magnetic measurements toward electrochemical magnets, J. Mater. Chem. C **2**, 5183 (2014).
[51] M. M. Thackeray, W. I. F. David, and J. B. Goodenough, Structural characterization of the lithiated iron oxides $Li_xFe_3O_4$ and $Li_xFe_2O_3$ ($0<x<2$), Mater. Res. Bull. **17**, 785 (1982).
[52] See the Supplemental Material at http://link.aps.org/supplemental/10.1103/PhysRevApplied.19.054022 for XRD patterns, FC and ZFC curves, MH curves, and the evolution of the magnetization for the battery without active material.
[53] L. Zhaohui, Z. Yongcheng, L. Xiangkun, G. Fangchao, Z. Leqing, L. Hengjun, X. Qingtao, L. Qinghao, Y. Wanneng, G. Chen, *et al.*, Reacquainting the electrochemical conversion mechanism of FeS_2 sodium-ion batteries by *operando* magnetometry, J. Am. Chem. Soc. **143**, 12800 (2021).
[54] X. Wei, C. Tang, Q. An, M. Yan, X. Wang, P. Hu, X. Cai, and L. Mai, $FeSe_2$ clusters with excellent cyclability and rate capability for sodium-ion batteries, Nano Res. **10**, 3202 (2017).
[55] X. Li, J. Su, Z. Li, Z. Zhao, F. Zhang, L. Zhang, W. Ye, Q. Li, K. Wang, X. Wang, *et al.*, Revealing interfacial space

charge storage of $Li^+/Na^+/K^+$ by *operando* magnetometry, Sci. Bull. **67**, 1145 (2022).

[56] W. Zhao, Z. Liu, Z. Sun, Q. Zhang, P. Wei, X. Mu, H. Zhou, C. Li, S. Ma, D. He, *et al.*, Superparamagnetic enhancement of thermoelectric performance, Nature **549**, 247 (2017).

[57] M. Gößler, M. Albu, G. Klinser, E.-M. Steyskal, H. Krenn, and R. Würschum, Magneto-ionic switching of superparamagnetism, Small **15**, 1904523 (2019).

[58] D. L. Leslie-Pelecky and R. D. Rieke, Magnetic properties of nanostructured materials, Chem. Mater. **8**, 1770 (1996).

[59] Z. H. Wang, D. Y. Geng, S. Guo, W. J. Hu, and Z. D. Zhang, Ferromagnetism and superparamagnetism of $ZnCoO:H$ nanocrystals, Appl. Phys. Lett. **92**, 242505 (2008).

[60] K. L. Livesey, S. Ruta, N. R. Anderson, D. Baldomir, R. W. Chantrell, and D. Serantes, Beyond the blocking model to fit nanoparticle ZFC/FC magnetisation curves, Sci. Rep. **8**, 11166 (2018).

[61] F. Freund, S. C. Williams, R. D. Johnson, R. Coldea, P. Gegenwar, and A. Jesche, Single crystal growth from separated educts and its application to lithium transition-metal oxides, Sci. Rep. **6**, 35362 (2016).

[62] Y. Singh, S. Manni, J. Reuther, T. Berlijn, R. Thomale, W. Ku, S. Trebst, and P. Gegenwart, Relevance of the Heisenberg-Kitaev Model for the Honeycomb Lattice Iridates A_2IrO_3, Phys. Rev. Lett. **108**, 127203 (2012).

[63] J. Hjorth, J. Sollerman, P. Moller, J. P. Fynbo, S. E. Woosley, C. Kouveliotou, N. R. Tanvir, J. Greiner, M. I. Andersen, A. J. Castro-Tirado, *et al.*, Beating the superparamagnetic limit with exchange bias, Nature **423**, 847 (2003).

[64] J. Sort, F. Garcia, S. Auffret, B. Rodmacq, B. Dieny, V. Langlais, S. Suriñach, J. S. Muñoz, M. D. Baró, and J. Nogués, Using exchange bias to extend the temperature range of square loop behavior in [Pt/Co] multilayers with perpendicular anisotropy, Appl. Phys. Lett. **87**, 242504 (2005).

[65] J. Liu, A. Singh, Y. Y. F. Liu, A. Ionescu, B. Kuerbanjiang, C. H. W. Barnes, and T. Hesjedal, Exchange bias in magnetic topological insulator superlattices, Nano Lett. **20**, 5315 (2020).

[66] Ò Iglesias, X. Batlle, and A. Labarta, Microscopic origin of exchange bias in core/shell nanoparticles, Phys. Rev. B **72**, 212401 (2005).